Journal of Materials Chemistry A

Functional SrF2 Coated Separator Enabling Robust and Dendrite-Free Solid Electrolyte Interphase on Lithium Metal Anode

Journal:	*Journal of Materials Chemistry A*
Manuscript ID	TA-ART-06-2019-006908.R1
Article Type:	Paper
Date Submitted by the Author:	13-Aug-2019
Complete List of Authors:	Li, Xing; Southwest Petroleum University, Liu, Yang; Southwest Petroleum University Pan, Y; Southwest Petroleum University Wang, Ming-Shan; Southwest Petroleum University, School of Material Science and Engineering Chen, Junchen; Southwest Petroleum University Xu, Hao; Southwest Petroleum University Huang, Yun; Southwest Petroleum University Lau, Leo; University of Science and Technology Beijing Shan, Aixian; University of Science and Technology Beijing Zheng, Jianming ; Dongguan Amperex Technology Ltd Mitlin, David; University of Texas at Austin

Table of contents

SrF_2 microsphere layer on separator could involve in the SEI formation and result in dendrite free SEI on lithium anode.

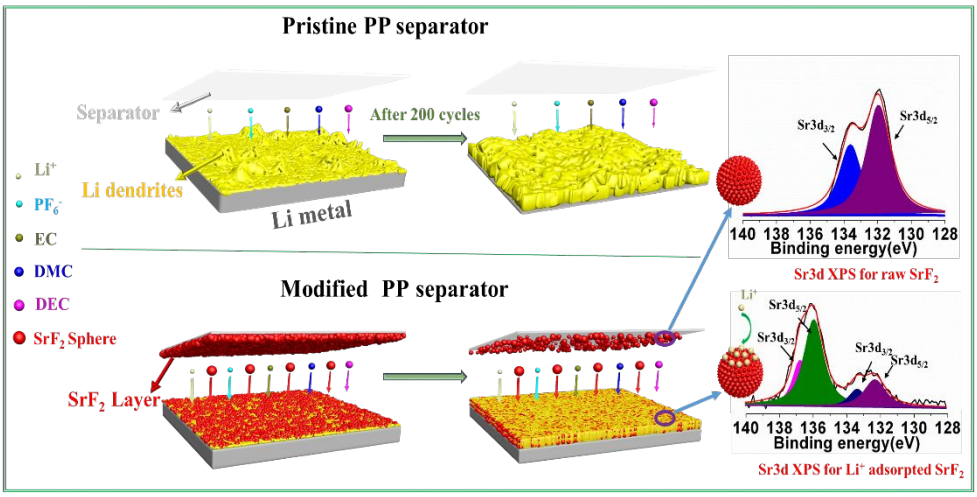

Functional SrF_2 Coated Separator Enabling Robust and Dendrite-Free Solid Electrolyte Interphase on Lithium Metal Anode

Xing Li[a*], Yang Liu[a], Yong Pan[a], Mingshan Wang[a], Junchen Chen[a], Hao Xu[a], Yun Huang[a], Woon Ming Lau[b], Aixian Shan[b*], Jianming Zheng[c*], David Mitlin[d*]

[a] *The Center of New Energy Materials and Technology, School of Materials Science and Engineering, Southwest Petroleum University, Chengdu, Sichuan 610500, China*

[b] *Center for Green Innovation, School of Mathematics and Physics, University of Science and Technology Beijing, Beijing 100083, China*

[c] *Research Institute (RI), NingDe Amperex Technology Limited, Ningde, Fujian 352100, China*

[d] *Walker Department of Mechanical Engineering, The University of Texas at Austin, Austin, Texas 78712-1591*

Corresponding authors: lixing@swpu.edu.cn (X.L.); axshan@ustb.edu.cn (A.S.); Zhengjm@atlbattery.com (J.M.Z.); David.Mitlin@austin.utexas.edu (D.M.)

Abstract:

An unstable solid electrolyte interphase (SEI) and accompanying Li metal dendrites are the key impediment to commercialization of high-energy lithium metal batteries (LMBs). We employ strontium fluoride (SrF_2) microspheres coated polypropylene (PP) separator to stabilize the SEI, and to prevent dendrites from growing. The approach was tested with Li||Cu half-cells, Li||Li symmetrical cells, and Li||NMC full LMBs, in each case, there being a major improvement. The Li||Cu cell with SrF_2 maintains a stable Coulombic efficiency CE of 80% after 100 cycles, when tested at 0.25 mA cm^{-2} to a capacity of 0.5 mAh cm^{-2}. By comparison, the uncoated PP baseline has a CE of 10% at cycle 60. The Li||Li cell with SrF_2 exhibits markedly smaller voltage polarization, and is able to stably cycle for approximately 340 hrs., *vs.* baseline that begins to display severe voltage instability at 200 hrs. The Li||NMC full LMB with SrF_2 shows an initial discharge capacity of 173 mAh g^{-1}, with 167 mAh g^{-1} (96.5%) being retained after 200 cycles at 200 mA g^{-1} (1C rate). The SrF_2 containing LMB also has a substantially improved rate capability over baseline, the difference being drastic even at the highest testing rate of 20C. First-principles calculations based on DFT indicate that lithium ions prefer to adsorb onto the SrF_2 surface, which should create a more uniform ion flux and reduce the propensity for dendrite nucleation. In parallel, the SrF_2 spheres bind

with the SEI layer, creating a tough *in-situ* formed composite membrane that mechanically stabilizes a planar metal interface.

Keywords: battery separator, ceramic coating, fluoride coating, dendrite blunting, dendrite prevention, solid state electrolyte (SSE), solid state battery (SSB)

1. Introduction

Lithium (Li) metal is regarded as the "Holy Grail" of negative electrode materials, serving as the basis for high energy Lithium Metal Batteries (LMBs). This is due lithium's reversible capacity that is ten times higher than that of graphite (3860 *vs.* 372 mAh g^{-1}), and its low electrochemical redox potential (-3.040 V *vs.* SHE) leading to a wide voltage window in full cell.[1-5] Having fallen out of favor for the last several decades due to catastrophic dendrite-related failures, LMBs are now again receiving intense scientific attention due to the need for gravimetric energies not possible with graphite anode-based lithium ion batteries (LIBs).[6, 7] However commercial applications for LMBs remain confronted by a series of severe challenges related to the instability of the lithium metal anode – electrolyte interface during repeated cycling and during fast charging. The interface instability is manifested as a number of severe problems, including early and steady-state low Coulombic efficiency (CE), cycling induced rise in impedance, swelling of flexible cells due to gas generation, and in the extreme cases anode to cathode electrical shorting leading to fire hazards.[8] Even if only a fraction (*e.g.* 30%) of the metal anode volume was stripped and then plated during each cycle, the overall volume change would still be three times larger than the 10% expansion/contraction associated with charging of graphite. This places severe demands on the solid electrolyte interphase (SEI), with its geometric stability being a necessary perquisite safe cell operation. Lithium metal – electrolyte interface instability is manifested as dendritic morphologies in various forms, often being dictated by the electrolytes employed, the charging rates, electrolyte additives, and metal hosts/supports that are present. Dendrite morphologies have been described as needlelike,[9, 10] moss-like,[11, 12] and treelike Li,[13-16], the more densely distributed moss-like structures believed to originate from base growth. Another integral part of a dendrite structure is the "dead Li", which is trapped and electrically isolated within the SEI layer, and hence permanently present for the remainder of the cycling regiment. [17] Before there is a future for LMBs outside the academic research laboratory, the lithium metal interfacial problem must be overcome.

The approaches to improve the interfacial stability of Li metal anodes could be broadly classified several categories, with multiple overlaps between each approach. One approach is to form LiX (X = Si, Ge, Sn, Sb *etc.*) alloys, in which the Li is in its ionic rather than metallic state.[18-23] In some cases, such as with Si or with Sn, the capacity of the anode is much higher than of graphite. While this has been the historical approach to increasing the capacity of the anode beyond that of graphite, it too suffers from the problem of extreme volume expansion (Si ~ 300%) that leads to SEI instability and all the associated issues. The second methodology is to manipulate the electrolyte chemistry to attempt to form a stable SEI layer on a Li metal surface. This includes the use of tailored Li salts, solvents, secondary electrolyte additives,[24-26] employing superconcentrated electrolytes,[27-30] nanostructured solid additives and passivating film coatings.[31-38] Researchers have also tuned the actual current collector, creating various secondary templates, supports and barrier layers to enable stable Li plating/stripping.[39-42] Another approach is substituting solid-state or hybrid liquid-solid electrolytes for fully liquid electrolytes. In principle, solid-state electrolytes (SSEs) are dendrite resistant due to their much higher elastic modulus that stops dendrite growth [39-45]. However even with solid-state cells, dendrites have been reported to grow along pore boundaries and other interfacial defects within the SSE.[50-52]

The focus of the current work is the methodology of tuning the polymer separator to stabilize the lithium – electrolyte interface during cycling. Typically, a conventional polymer separator is coated with nanomaterials with tuned structure, geometry and chemistry that regulate Li ion flux, promoting uniform deposition and stripping, as well as more effectively pushing back against any dendrites that do begin to grow.[53-61] Recent exciting studies have demonstrated that the modification of separator strategy is highly effective for improving the performance of Li metal anodes.[62,63] Examples of approaches with significant improvement in metal anode stability include layer-by-layer assembly of polyethylene oxide (PEO) composite membrane with pores finer than the dendrite dimensions,[64] and an elastomeric solid-electrolyte separator that mechanically blocks dendrite motion.[65] Coating the separator by materials with sufficient mechanical strength (Modulus, toughness) to block dendrites has been shown to be effective. Nanostructured coatings or macroscopic secondary barriers include N,S-co-doped graphene nanosheets,[66] Al_2O_3,[67] conductive polymers,[68] Kimwipe paper,[69] functionalized nanocarbon,[70] among others tailoring Li metal anode size,[71] modifying separator with Polydopamine and uniformly distributing Li-ion flux through

nanochannel confinement.[72,73] Separators coated with ZrO_2/POSS and 3D porous ZSM-5 have also been shown as effective. [74-77] These coatings exhibit a high ionic conductivity, promoting a more uniform flux of Li than what occurs when Li moves solely through the open pores of the underlying polymer membranes.

In this work, a layer of strontium fluoride (SrF_2) microspheres was coated onto the side of a polypropylene (PP) separator facing the Li metal, with its effect on suppressing dendrite growth being thoroughly studied by combined experiment and modeling. The SrF_2 coating layer was initially selected on the basis of its high elastic stiffness, as well as its chemical and electrochemical stability relative to the electrolyte.[78, 79] These features allow it to act as an excellent mechanical protection layer, minimizing or even fully preventing the physical penetration of Li dendrites through the separator. In the process of testing and analysis, we observed that the SrF_2 microspheres were also highly effective in tuning the solid electrolyte interphase (SEI) during electrochemical cycling. Hence the SrF_2 coating possessed a potent role in actually suppressing the early growth of dendrites, which is driven by excessive SEI formation.[42,52] The fundamental mechanisms for the observed improvements were systematically investigated through X-ray Photoelectron Spectroscopy (XPS) analysis combined with Density Functional Theory (DFT) simulation.

2. Experimental Section

Materials Synthesis and Coating of Separator

The SrF_2 microspheres were prepared by a one step hydrothermal reaction approach. A 0.1 mol/L of strontium nitrate ($Sr(NO_3)_2$) and 0.05 mol/L sodium tetrafluoroborate ($NaBF_4$) aqueous solution separately synthesized. Then 0.2 mol trisodium citrate ($C_6H_5Na_3O_7$) was added into the $Sr(NO_3)_2$ solution as a dispersant, followed by adding the as-prepared $NaBF_4$ solution dropwise while vigorously stirring. The resultant product was hydrothermally treated in a polytetrafluoroethylene (PTFE) lined autoclave at 180 °C for 12 hrs. The sample was then cooled to room temperature, centrifugally washed with deionized water, and subsequently dried at 80 °C overnight to obtain the SrF_2 microspheres. The precursors $Sr(NO_3)_2$, $NaBF_4$ and $C_6H_5Na_3O_7$ were purchased from Shanghai Macklin Biochemical Co. Ltd. A commercial PP separator (Celgard 2400, 25μm) was employed. The separator coating was based on a slurry of 90wt% as-prepared SrF_2 microspheres and 10wt% poly (vinylidene fluoride) (PVDF), which were intimately mixed using NMP solvent as the dispersant. The

viscous slurry was then cast onto the Li metal facing side of a conventional polypropylene (PP) separator using a doctor blade technique. The loading amount of SrF_2 microspheres on the surface of the PP separator was about 1.0 mg/cm^2. The SrF_2 microspheres coated PP separator was further dried at 60 °C under vacuum overnight.

Analytical Characterization

Powder X-ray diffraction XRD (Panalytical X'pert MPD DY1219, Cu K_α radiation) was employed to characterize the crystal structure of the as-prepared SrF_2 microspheres. The morphologies of the SrF_2 microspheres and the SrF_2 microspheres coated onto the PP separator were also characterized by scanning electron microscopy (SEM, Hitachi SU8010). Surfaces and the cross-sections on the Li metal anodes with different Li deposition thickness and cycle numbers were also characterized by the SEM analysis. X-ray photoelectron spectroscopy (XPS, Phi 5000 Versaprobe iii) was conducted to analyze the solid electrolyte interphase (SEI) composites on the Li metal surfaces

Electrochemical Characterization

Electrochemical analysis was carried out using CR2032 coin cells (MTI Corporation). The cycling and rate performance of the cells was evaluated using BTS-5V20mA cell galvanostatic testing instruments (NEWARE Electronic Co., Ltd). The coin cell assembly was conducted in a high-purity argon filled glove box with the water and oxygen contents both less than 0.1 ppm. Unless otherwise stated, tests were performed at 30°C. However, the Supplemental figures list some results where testing was performed at 60°C instead. The coated separator was tested in a symmetrical Li metal – Li metal (termed "Li||Li") and Li – Cu (termed "Li:Cu") current collector configuration. The Li metal anodes were purchased from MTI Corporation. The electrolyte for the Li||Cu and Li||Li coin cells was 1 mol/L $LiPF_6$ - EC:DEC:DMC (1:1:1). The Li||Cu cells were tested at charge/discharge current density of 0.25 mA cm^{-2} and a deposited capacity of 0.5 mAh cm^{-2} with a voltage range of 0 - 1 V. The Li||Li cells were tested at a current density of 0.25 mA/cm^2 and a charge/discharge capacity of 0.5 mAh cm^{-2}. The SrF_2 coated separator was also tested in a full-cell configuration versus an NCM ($LiNi_{0.68}Co_{0.1}Mn_{0.22}O_2$) cathode previously reported.[80] An electrolyte solution of 1 mol/L $LiPF_6$ - EC:DEC:DMC (1:1:1 by vol.) electrolyte was employed. In all cases, only one side of the separator was coated by the SrF_2 microspheres, in the full cell and Li||Cu being the side that faced the Li metal.

The full cell cathode containing 90wt% NCM, 5wt% poly (vinylidene fluoride) (PVDF) and 5wt% acetylene black (AB). The amount of active material (NCM) in the cathode was about 5 mg/cm^2. For the full cells the voltage range was 2.7–4.4 V. For the Li||NCM cells, commercial battery representative constant-current charge followed by a constant-voltage charge to 4.4 V was used for the charge step. Current densities of C/10, C/3, 1C, 2C, 3C, 5C, 10C and 20C were employed for the Li||NCM coin cells testing, where 1C = 200 mA g^{-1} (capacity of $LiNi_{0.68}Co_{0.1}Mn_{0.22}O_2$ at 20 mA g^{-1}). Electrochemical impedance spectroscopy (EIS) was performed on the cells after different cycle numbers using CH Instruments CHI660D. Measurement was performed in the charged state of 4.1 V, at the frequency ranging from 10^5 to 10^{-2} Hz, with a potential perturbation amplitude of 10 mV.

3. Results and Discussion

As-synthesized Materials

Figure S1(a) and **(b)** present the morphology of the as-prepared SrF_2 microspheres, which range in diameters from sub-1 micrometer to about 5 micrometers. Shown are SEM images of the as-synthesized SrF2 microspheres, taken at different magnifications (scale bars on bottom right). According to the higher magnification image in **Fig. S1(b)**, it may be observed that microspheres consist of an assembly of sub-100 nm crystallites, interspersed with nanoporosity. **Figure S1(c)** demonstrates that the X-ray diffraction peaks of the as-prepared sample corresponds well to the pure equilibrium phase of SrF_2 (Fm-3m #225 a = 0.57996 nm) , as referenced to the SrF_2 PDF card (# 06-0262). **Figures S2(b)** and **(c)** show the SEM images of the pristine PP separator and of the SrF_2 microspheres coated PP separator, respectively. It may be observed that the SrF_2 microspheres completely and uniformly coat on PP separator surface. A high degree of lithium ion permeable pathways are expected to be present in the coating both due to the microscopic spacing between the particles and due to the nanopores within the individual nanocrystallites. The SrF_2 microspheres coated PP separator was further characterized to analyze the effect on the porosity and the pore size distribution, comparing these results with the original PP separator. **Figure S3(a)** and **(c)** compare the nitrogen isotherm absorption-desorption curves of the pristine *vs*. the coated separators. **Figures S3(b)** and **(d)** compare the corresponding pore size distributions. It could be observed that the total surface area and pore volume (S_{BET}, $V_{total/BJH}$) as well as the Average Pore Distribution (APD) for the SrF_2 coated separator is larger than

for the baseline, agreeing with the SEM images that show extensive open nanoporosity within the spheres.

Electrochemical Performance

The Li||Cu half-cells and Li||Li symmetric cells with the pristine PP (baseline) and the SrF_2 microspheres coated PP separators were evaluated to compare the Coulombic efficiency (CE), the overall cycling stability, and the voltage polarization evolution. These results are shown in **Fig. 1**. **Figure 1(a)** shows a comparison of the cycling CE of Li||Cu cells that were tested at 0.25 mA cm^{-2} between 0 – 1 V vs. Li/Li^+. For each cycle, the total plating/stripping capacity was 0.5 mAh cm^{-2}. It may be observed that during the first 10 cycles, with the pristine PP and the SrF_2 microspheres coated PP separators the CE are almost the same at about 80%. However, with increasing cycle number, the CE with pristine PP separator beings to rapidly degrade, going to about 10% after the 60 cycles. Without surface modification, the vast majority of the Li becomes trapped in the solid electrolyte interphase (SEI) structure that forms on the Cu at cycle 1 and subsequently grows with every cycle. In contrast, the CE values with the SrF_2 coating remains at 80% at cycle 100. We should point out that the Li||Cu half-cell represents the most aggressive method for testing metal - electrolyte instabilities and that the CE values using both symmetric Li||Li cells and full Li||NCM batteries are higher. This is likely due to the bare Cu current collector being itself catalytic towards SEI formation and because at every cycle all the Li metal is fully stripped, leaving behind only remnant SEI on the Cu. The mechanistic origin of the major CE improvement due to the SrF_2 coating will be discussed shortly.

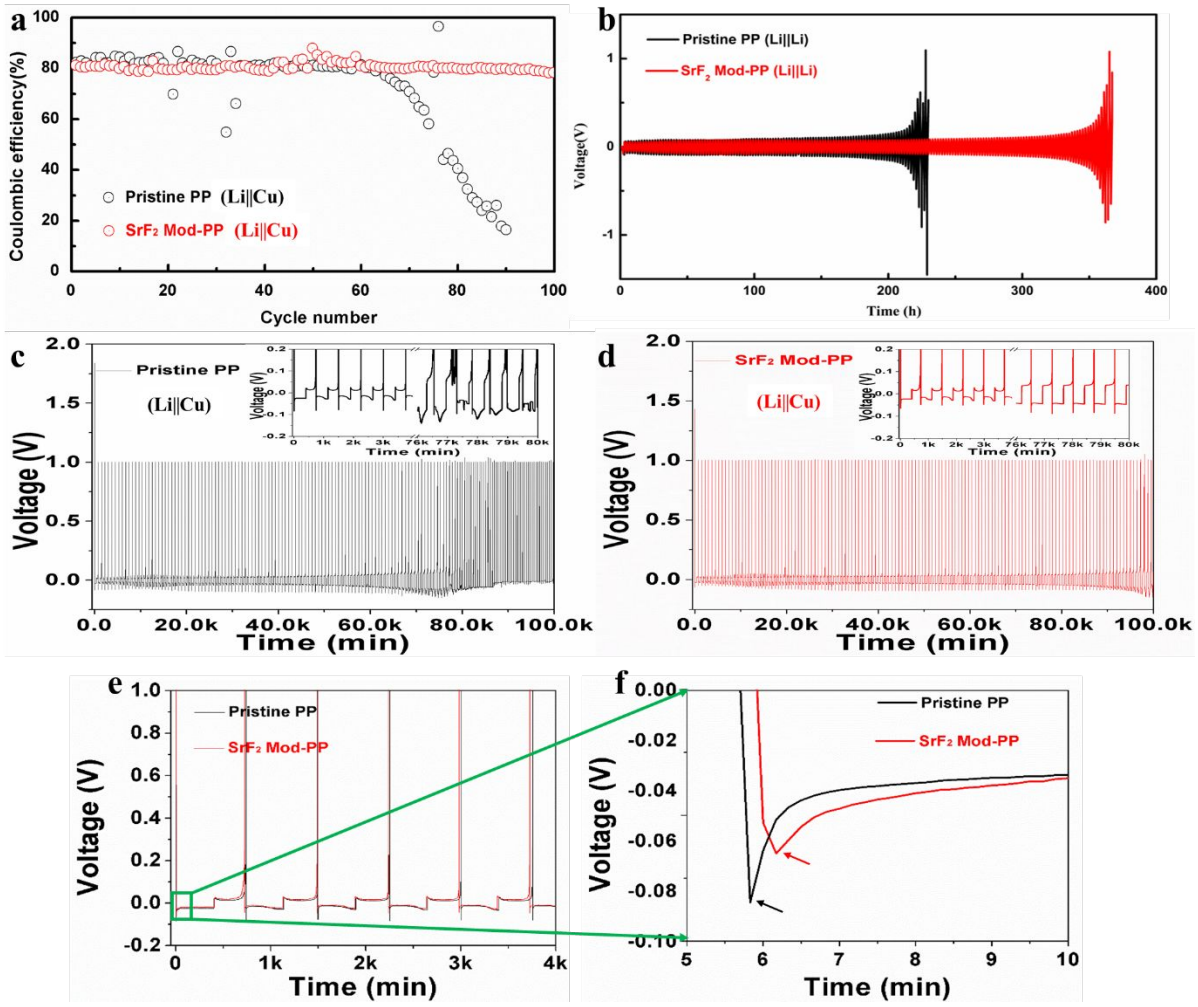

Figure 1 Comparison of the baseline pristine (unmodified) PP and the SrF_2 coated PP separators in half-cell and symmetrical cell configurations. **(a)** A comparison of the cycling Coulombic efficiency (CE) of Li||Cu cells, tested at 0.25 mA cm^{-2} between 0 – 1 V vs. Li/Li^+ to a capacity of 0.5 mAh cm^{-2}. **(b)** Cycling performances of Li||Li cells, tested at a current density of 0.25 mA cm^{-2} to a capacity of 0.5 mAh cm^{-2}. **(c), (d)** Voltage *vs.* time curves for the Li||Cu cells, with insets showing selected enlarged examples of the curves. **(e), (f)** Comparison of voltage *vs.* time curves for the Li||Cu cells at cycle 1.

Figure 1(b) shows cycling behavior of symmetrical Li||Li cells, the focus being the onset of voltage instability and the degree of polarization of the cathodic (plating) sweeps. In **Fig. 1(b)** the cycling performances of Li||Li cells was evaluated at a current density of 0.25 mA cm^{-2} to a capacity of 0.5 mAh cm^{-2} per cycle. The enlarged voltage-time plots are shown in Figure S4, which demonstrates that there are no soft short circuits for the cells. Moreover, the SrF_2 microsphere coated PP separator could make the Li||Li coin cells cycle for ca. 350 hrs, which is 150 hrs longer than the pristine PP separator. This further demonstrates that the SrF_2 microsphere coating layer could facilitate the formation of a more stable SEI on the Li metal,

which is favorable for reducing the electrode polarization and hence improving the cycling stability. A highlight the voltage *vs.* time behavior for Li||Cu cells is shown in **Figs. 1(c)** and **(d)**, with insets showing selected enlarged examples of the curves. These magnified images of early cycling behavior demonstrate the key difference in the planting overpotential with SrF_2 coated *versus* pristine separators. An onset of severe voltage instability may be qualitatively associated with the onset of severe SEI formation and the associated growth of metal dendrites. In turn the dendrites catalyze more SEI growth on their surface, forming a feedback loop that in a real battery would lead to shorting or catastrophic rise in cell impedance. Even at cycle 1 (**Fig. 1(e)**, **(f)**), the cathodic (plating) overpotential is smaller with the SrF_2 coating, being - 0.065 V vs. - 0.084 V. This indicates that the role of the coated separator goes far beyond just blocking the growth of "mature" dendrites, rather altering the early stage SEI formation kinetics. This critical aspect will be discussed in detail further in the manuscript.

Figure 2(a) shows the long-term cycling performance and the corresponding galvanostatic charge-discharge profiles of Li||NCM cells using the prestine separator and the SrF_2 coated PP separator. **Figure 2(a)** provides a master plot of the cycling capacity retention (left axis) and associated CE (right axis). Testing was performed between in the batter-representative range of 2.7-4.4 V at C/3 (1C = 200 mA g^{-1}). Prior to that current density regimen, three formation cycles at C/10 were done. **Figures 2(b)** and **(c)** provide the actual galvanostatic charge-discharge profiles from which Fig. 2(a) was derived. **Figure 2(d)** provides a rate capability comparison at currents ranging from C/10 to 20C, while **Figs. 2(e)** and **(f)** show the corresponding galvanostatic data. The Li||NCM coin cell with the pristine separator shows an initial discharge capacity of 198 mAh g^{-1} and a CE of 85.1%. At 1C rate, its discharge capacity is 174 mAh g^{-1}, which fades to 157 mAh g^{-1} after 200 cycles, corresponding to a capacity retention of 90.2%. In contrast, for the Li||NCM cell with the SrF_2 coated separator, the initial discharge capacity is 209 mAh g^{-1} with an initial CE of 88.6%. At 1C, its discharge capacity is 173 mAh g^{-1}. The small but not trivial difference in the initial discharge capacities - CEs of the two architectures is important. It highlights the role of the SrF_2 modification in influencing early kinetics, prior to when dendrites are likely to exist or at least be large enough to be influential. Rather, at early cycles, the SrF_2 coating affects the SEI formation kinetics and other ion transfer processes from the cathode to the anode and vise-versa. After 200 cycles, the discharge capacity of the SrF_2 coated specimen is 167 mAh g^{-1}, corresponding to a capacity retention of 96.5%.

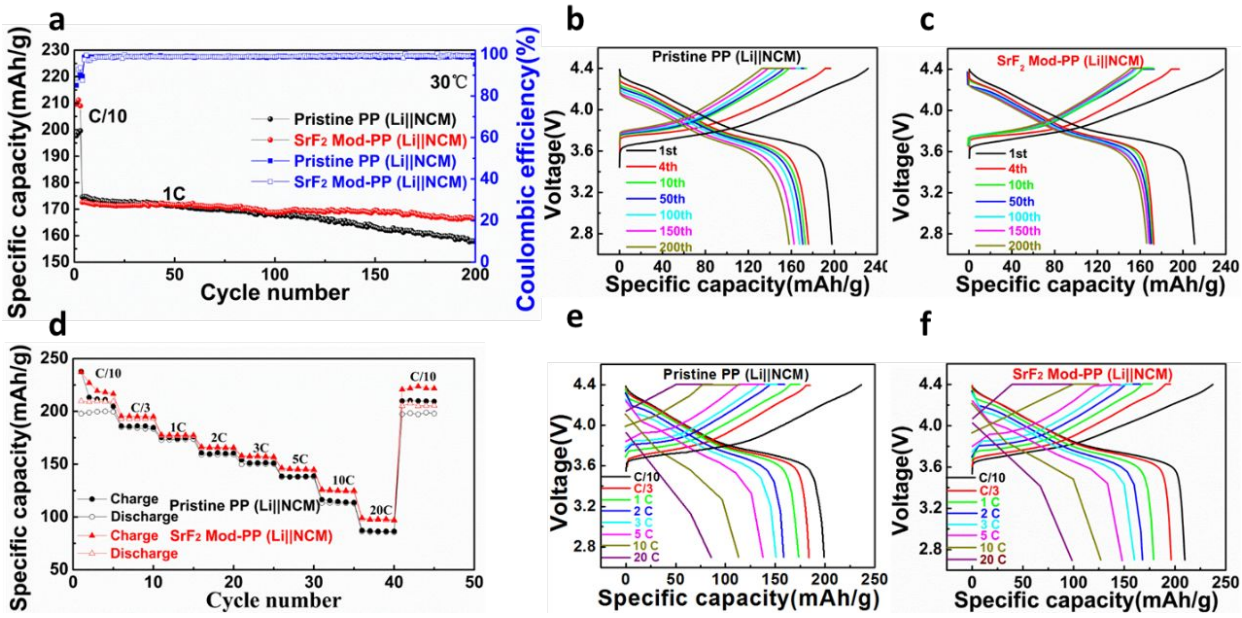

Figure 2 Galvanostatic performance of Li||NCM cells with and without the SrF_2 separator coating. **(a)** Cycling capacity retention and CE comparison, with testing being performed between 2.7 and 4.3 V at C/3 (1C = 200 mA g^{-1}), after the three formation cycles at C/10. **(b)** and **(c)** Corresponding galvanostatic charge-discharge profiles. **(d)** Rate capability comparison at C/10 to 20C. **(e)** and **(f)** Corresponding galvanostatic data.

Comparing **Figs. 2(b)** and **(c)**, the Li||NCM cell using the SrF_2 coated PP separator demonstrates a smaller polarization at different stage of cycling. We attribute this to a more stable SEI layer with the SrF_2, which at a given cycle is thinner and should yield a lower resistance at every charge - discharge cycle. This conclusion is in agreement with the Li||Li cell results, where the same trend is observed. Extended cycling performance of Li||NMC cells with and without SrF_2 was also evaluated at a current density of 2C and an elevated temperature of 60 °C. These results are shown in **Fig. S5**. The initial reversible capacity for the SrF_2 containing Li||NCM cell is 189 mAh g^{-1}. After 200 cycles, this value is 155 mAh g^{-1}, corresponding to a capacity retention of 82.0%. The reversible capacity for prestine Li||NCM cell is 182 mAh g^{-1}, degrading to 125 mAh g^{-1} after 200 cycles, *i.e.* a retention of 67.6%. The SrF_2 containing Li||NCM also exhibits smaller polarization at different stage of cycling.

Figure 2(d) shows the rate capability and the corresponding galvanostatic charge-discharge curves of Li||NCM cells with pristine and SrF_2 coated separator. The reversible capacity for the Li||NCM cell with the SrF_2 separator is are 210, 193, 177, 165,

157, 145, 125, and 97 mAh g^{-1} at C/10, C/3, 1C, 2C, 3C, 5C, 10C, and 20C respectively. These are higher than the Li||NCM with the uncoated separator, being 198, 185, 173, 159, 150, 137, 113 and 85 mAh g^{-1} at the same currents. An improved rate capability of a full cell, especially at the higher currents could also be related to a lower SEI-related cell resistance. Battery cell electrochemical kinetics are known to drop off with SEI growth, which causes progressively increasing polarization during repeated charging - discharging. A number of factors get worse as the SEI thickens, including ion diffusional limitations within the layer, and increased charge transfer resistance.

Cycled Li Metal Anodes

The morphological and surface structure/chemistry evolution of the post-cycled Li metal anodes were systematically investigated, comparing the SrF_2 coated *versus* the pristine separator. **Figure 3** shows top-down SEM images of the post-cycled Li anode surfaces, directly comparing the two architectures at various testing conditions. The analyzed specimens were the Li metal anodes tested in a full cell Li||NCM configuration. **Figures 3(a) - (e)** show pristine *vs.* **(f) - (j)** SrF_2 modified anode, plated at 20 mA g^{-1} for 1h, 2h, 4h, 8h and 10h, corresponding to total capacity of 20, 40, 80, 160 and 200 mAh g^{-1}. It is worth noting that for the first cycle of charging at the C/10 formation cycles, the there is more Li plated/stripped (*i.e.* higher reversible capacity) than during subsequent higher rate cycling.

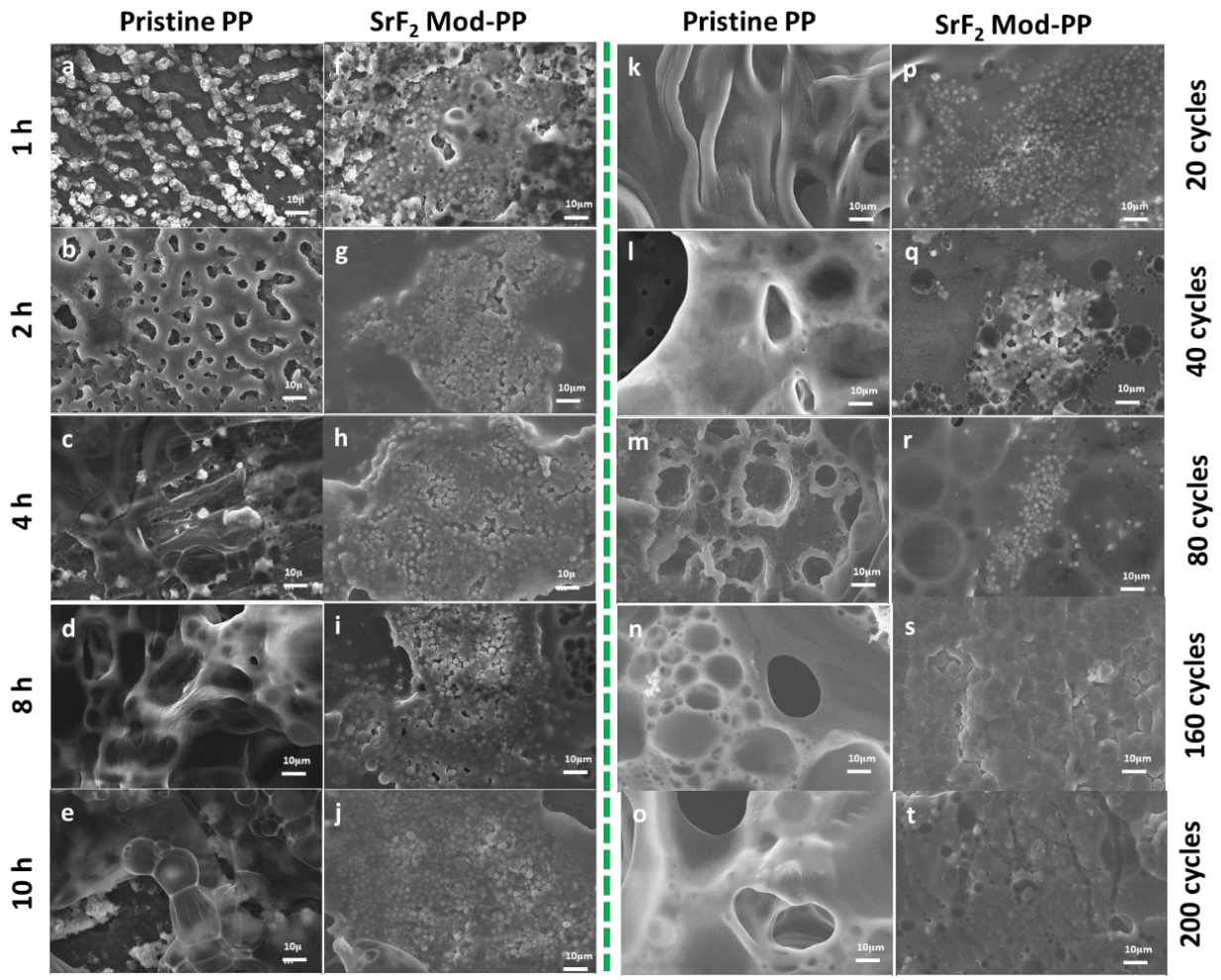

Figure 3 SEM images of the surface morphologies of the post-cycled Li metal anodes tested in a full cell Li||NMC configuration, comparing pristine vs. SrF_2 modified separators. **(a)** - **(e)** pristine *vs.* **(f)** - **(j)** SrF_2 modified, plated at 20 mA g^{-1} for 1h, 2h, 4h, 8h and 10h, corresponding to total capacity of 20, 40, 80, 160 and 200 mAh g^{-1}, respectively. **(k)** - **(o)** Pristine vs. **(p)** - **(t)** SrF_2 modified, tested for 20, 40, 80, 160 and 200 cycles at 200 mA g^{-1} for 2 hrs. per cycle.

Per **Fig. 3(a)** with the pristine baseline, after 1 hour there are isolated islands forming on the surface of Li metal anode. These have been attributed to early-stage formation of a non-uniform SEI structure.[81, 82] Such structure would be ultimately associated with dendrite formation since it would result in highly non-uniform mechanical properties and ion diffusion characteristics of the SEI layer. The observation of early-stage heterogeneities also leads to the conclusion that Li metal growth instabilities occur quite early in the process, significantly earlier than what may be detected from conventional galvanostatic data. The time, the surface instabilities in the baseline become more severe, leading to a highly roughened surface after 8 hours. Although the Li metal - SEI morphology does not directly correlate with classical

lath-like isolated dendrites known to lead to catastrophic shorting, such a morphology has been observed prior, e.g. ref.[83] A highly roughened metal surface with a thick SEI layer will ultimately lead to unacceptable levels of charge - discharge polarization and would kill the cell nevertheless. With the SrF_2 coating, the Li metal morphology still roughens with cycle number, but at a much-reduced rate. Even after 10 hours of cycling the surface is relatively flat, per **Fig. 3(j).**

One important observation regarding the SrF_2 coated samples is that a layer of microspheres is lodged within the SEI layer at all cycle numbers analyzed. The spheres were observed in all micrographs of the Li metal surfaces and confirmed by the XPS results shown in **Fig. 5** and **Fig. S14**. This gives a strong indication that the SrF_2 microspheres are directly involved in SEI growth kinetics, rather than just acting as a secondary mechanical strengthening layer to block mature dendrites from piercing the separator. One may consider the role of the SrF_2 microspheres as that of rigid filler inside the outer SEI layer that is known to be primarily organic. A membrane of an organic SEI with embedded ceramic SrF_2 particles is classic "soft-hard" composite system, based a ductile matrix and rigid non-deformable filler. Such systems are expected to be physically tough, displaying a combination of strength and ductility. It exerts an effective counterforce to prevent the electrolyte interface from geometrically roughening at early stages, before dendrites have a chance to grow. This composite is formed *in-situ* during cycling as early SEI growth causes it to bind to the SrF_2 sitting on the contacting separator.

Figures 3(k) - (o) show an analogous comparison but with pristine *vs*. SrF_2 modified full cells, tested for 20, 40, 80, 160 and 200 cycles at 200 mA g^{-1} for 2 hours per cycle. The trend is nearly identical. With the pristine separator, the Li metal surface begins to roughen early in its cycling life and is quite morphologically heterogenous even by cycle 40. Conversely, with the SrF_2 coating the morphology is relatively flat even at cycle 200. **Figure S6** shows SEM images of the cross-sections of the post-cycled Li metal anodes from Li||NCM cells. Figures **S6(a) – (e)** highlight the pristine separator, while **(f) – (j)** show the SrF_2 coated separator. These results further highlight the drastic difference in the post-cycled morphology. A highly roughened SEI layer in the baseline is directly contrasted to a substantially smoother metal at identical cycle number with the separator coating. The SrF_2 coating was also effective in

stabilizing the Li metal surface at 60 °C and 400 mA g^{-1}. The top-down and cross-section SEM views comparing the two formed SEI surfaces morphologies are shown in **Figs. S7(a) - (d)**, highlighting the effectiveness of the SrF_2 even at high temperatures.

Figure S8 compares the pristine vs. coated separators in the as-synthesized state and after cycling. **Figure S8 (a)** and **(b)** show low magnification photographs of the pristine and the SrF_2 coated separators in the uncycled state, respectively. The pristine separator is in the as-received state, while the SrF_2 modified separator is completely coated with no visible holes. **Figures S8(c)** and **(d)** contrast the post-cycled Li metal anodes, again highlighting the major differences in the morphologies. **Figures S8(e)** and (f) show the post-cycled pristine separator and the SrF_2 coated separator. The baseline uncoated separator shows clear evidence of SEI adhesion in the form of dark debris covering the surface. Remarkably, the post-cycled SrF_2 coated separator is completely clean, with no evidence or either the SEI of the ceramic microparticles. This further supports the argument that the microspheres are directly incorporated into the growing SEI layer.

The cycled Li||NCM cells with the pristine versus the SrF_2 coated PP separators were further analyzed using electrochemical impedance spectroscopy (EIS). **Figure 4** displays Nyquist plots of Li||NCM coin cells after 10th, 20th, 40th, 80th, 160th, and 200th cycles, tested at 200 mA g^{-1} for 2 hrs. per cycle. **Figures 4(a)** and **4(b)** show the pristine separator results, while **(c)** and **(d)** highlight the SrF_2 coated separator results at identical test conditions, with **(b)** and **(d)** showing enlarged views of the high-frequency region. In all cases, the impedance spectra were collected at a fully charged state of 4.1 V. The insets in **(a)** and **(c)** show the equivalent circuits used for fitting the experimental data. The Nyquist plots contain two semicircles, the higher frequency semicircle representing the SEI impedance R_{SEI} and lower frequency semicircle representing the charge transfer impedance R_{CT}.[84-88] The intercept at the high frequency with the real axis corresponds to the electrolyte resistance (R_E), although strictly speaking it also includes a summation of the Ohmic resistances of various portions of the cell.[89, 90] The results of the fits are shown in **Table1.**

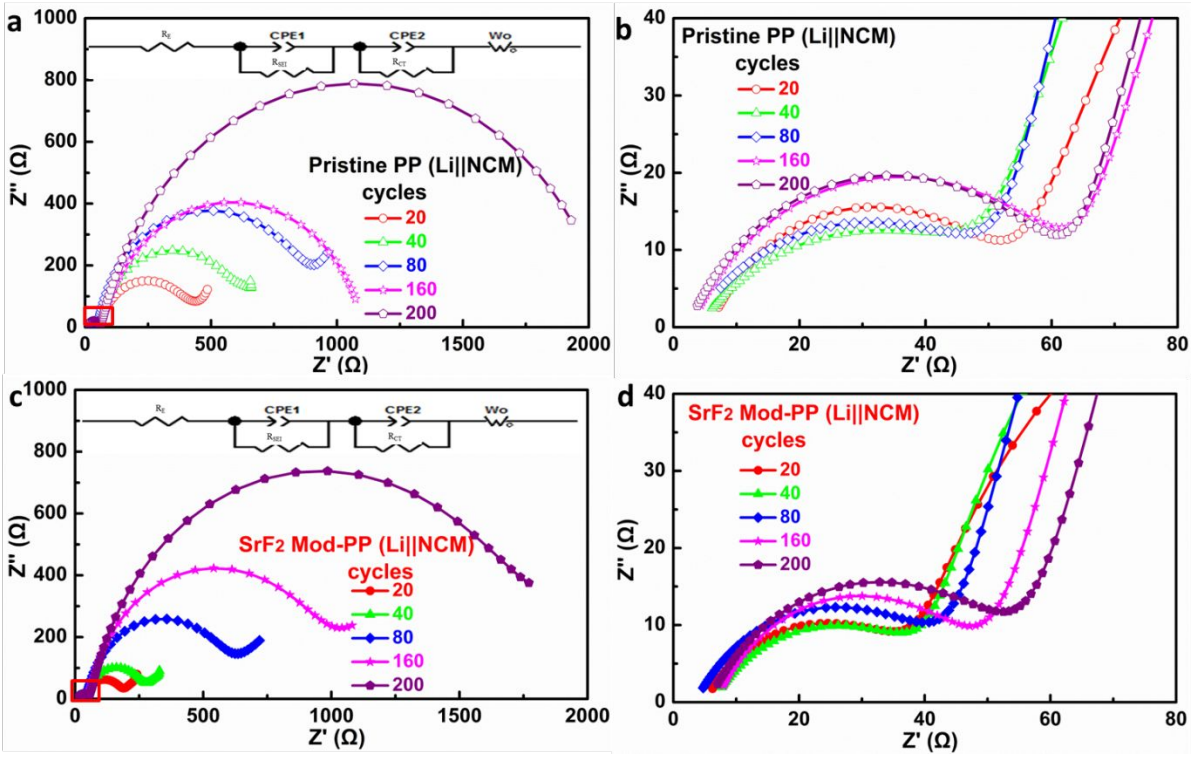

Figure 4. Nyquist plots of Li||NCM coin cells 10th, 20th, 40th, 80th, 160th, and 200th cycles at 200 mA g^{-1} for 2 hrs. per cycle. **(a)** and **(b)** pristine, **(c)** and **(d)** SrF_2 coated separator, with **(b)** and **(d)** showing enlarged views of the high-frequency region. The impedance spectra were collected at a charged state of 4.1 V.

Table 1. Fitted parameters for the experimental EIS spectra, using the equivalent circuit shown in the inset of Figure 4.

samples		20^{th} cycles	40^{th} cycles	80^{th} cycles	160^{th} cycles	200^{th} cycles
Pristine PP	R_E	5.6	5.8	5.9	6.2	6.4
	R_{SEI}	46.7	50.7	52.5	62.1	62.9
	R_{CT}	312.1	532.7	816.7	1040.0	2025.0
SrF_2 Mod-PP	R_E	5.4	5.5	5.7	6.1	6.2
	R_{SEI}	34.8	35.7	39.9	41.0	49.7
	R_{CT}	130.3	212.9	500.3	829.3	1599.0

The difference in both resistances is substantial and correlates well to the contrasting Li anode morphologies, shown in the previous figure. With the pristine separator the R_{SEI} values are 46.7, 50.7, 52.5, 62.1, 62.9 ohms, at 20^{th}, 40^{th}, 80^{th}, 160^{th}, 200^{th} cycle, respectively. The corresponding R_{SEI} values with SrF_2 are 34.8, 35.7, 39.9, 41.0, 49.7 ohms. The R_{CT} values for using the prestine separator are 312.1, 532.7, 816.7, 1040.0, 2025.0 ohms, at 20^{th}, 40^{th}, 80^{th},

160th, 200th cycle, respectively. The corresponding R_{CT} values for using the SrF_2 coated separator are also lower, being at 130.3, 212.9, 500.3, 829.3, 1599.0 ohms. **Figure S9** presents the Nyquist plots after 100th cycles at 2C and 60 °C. The R_E, R_{CT} and R_{SEI} values with the pristine separator are 10.2, 244.9 and 4800 ohms. The corresponding values with SrF_2 are 4.1, 143.6 and 167.4 ohms. This is even more of a drastic difference and may be attributed to the higher rate of SEI growth at elevated temperatures.

Figures S10 and S11 present the XPS survey spectra of Li metal anodes after different Li deposition times of 1 h, 2 h, 4 h, 8 h, 10 h, or electrochemical cycles of 20, 40, 80, 160 and 200. These conditions are the same ones employed for analysis in **Fig. 3**. **Figures S12 and S13** present the high-resolution spectra of C1s and O1s for these test conditions. The SrF_2 microspheres did not affect the species detected in the SEI, which is reasonable since the same electrolyte was employed in both cases. The SEI films contain the same components of the carbonyl group (~289.0 eV (C=O)), hydrocarbon (~285.0 eV (C-C/C-H)), and carbide species (~283.0–283.5 eV) in C 1s spectra, and the carbonyl (~531.0 eV (C=O))/ether oxygen (~532.0 eV (C-O-C)) in O 1s spectra.[91, 92] The carbonyl group likely originated from decompositions of the carbonate solvents.[7] The dominating carbide species, for example, $LiCH_2CH_2OCO_2Li$ comes from the reduction of EC.[91]

There was a notable difference in the relative amounts of some components for the pristine *vs.* SrF_2 modified separator. The high-resolution spectra of F1s and Sr3 are shown in **Fig. 5**. At differing deposition times and cycle numbers, the intensity of the $Li_xPF_yO_z$ and LiF signals (decomposition of $LiPF_6$) with the uncoated separator are stronger than when SrF_2 is employed. A similar effect was reported with other functional separator coating layers. The carbide species in the SEI with the SrF_2 layer displayed a higher intensity. It has been reported that a higher relative level of carbide species is associated with a more stable SEI film.[91] The order of causal relationship requires further investigation: Does SrF_2 promote carbides, or are carbides an outcome of SrF_2 stabilizing the SEI by other chemical - physical means? One possibility is that the F derived from SrF_2 microspheres induces more EC solvent reduction at the initial stage.[1] As reported in our previous work,[7] more EC solvent reduction is also favorable to form a robust SEI film. As shown in **Figs. S12(k) - (o)**, with the pristine separator, the carbonyl group signal becomes progressive weaker with cycling. By comparison, this occurs less in the presence of SrF_2, as shown in **Figs. S12(p) - (t)**. This

effect needs further investigation and may be related to preferential consumption of a distinct species within the solvent during the more excessive SEI growth on the metal surface of the baseline. Moreover, the high-resolution spectra of Sr3d demonstrates that the SrF_2 microspheres are trapped within the SEI. As compared with the Sr3d high resolution spectra of the as prepared SrF_2 (**Fig. S15**), the peaks from the SEI entrapped SrF_2 shows higher peak energies.

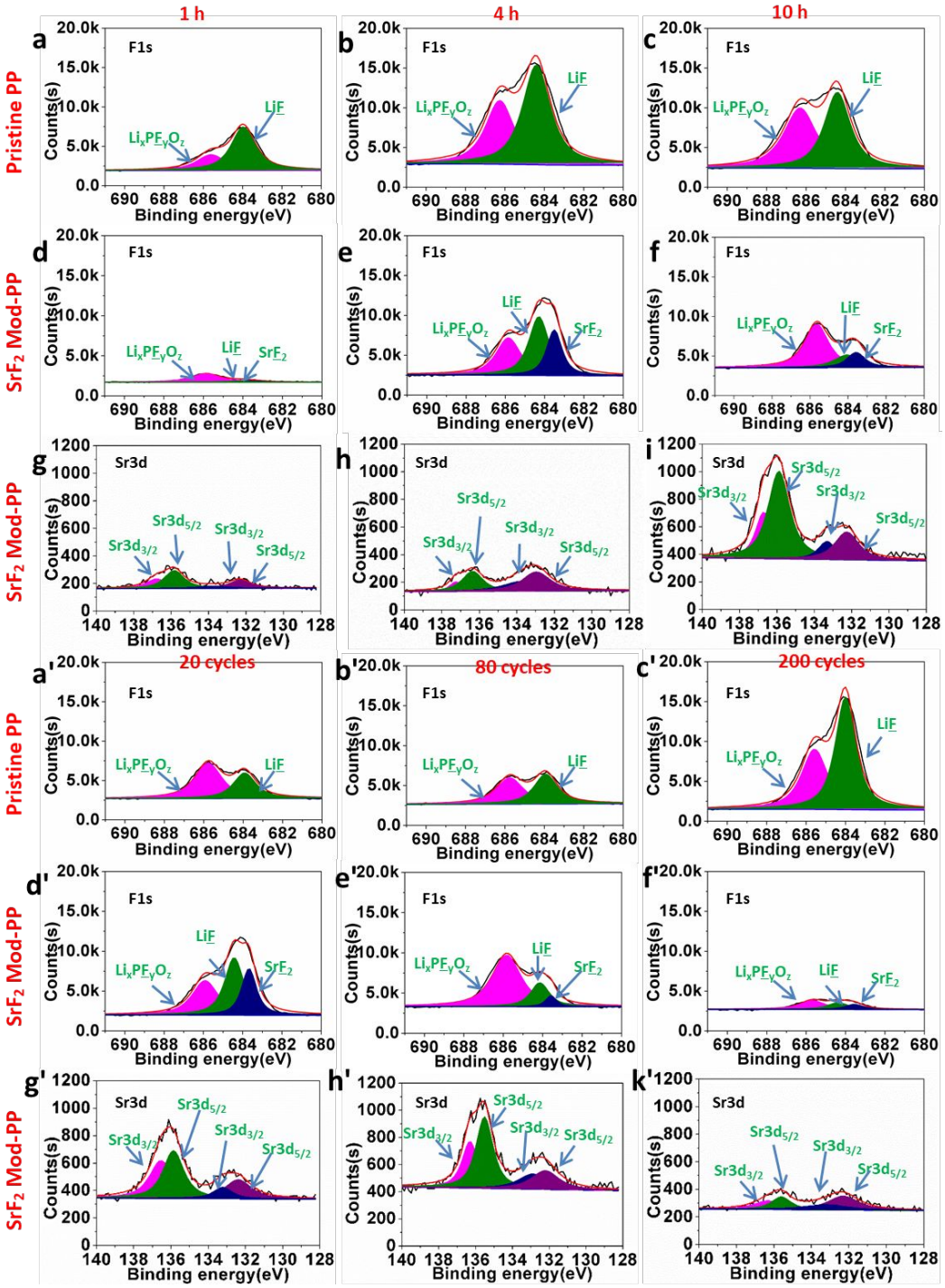

Figure 5. (a) - **(i)** and **(a')** - **(i')** High – resolution XPS spectra for post-cycled Li metal anodes with pristine vs. SrF_2 modified separator. **(a)** - **(i)** Testing conditions are the same as in **Fig. 3**, 20 mA g^{-1} for 1h, 4h, 10h. **(a') – (i')** Tested for 20, 80, and 200 cycles at 200 mA g^{-1} for 2 hrs. The survey spectra and the high-resolution XPS data 2 hr. and 4 hrs., 40 cycles and 160 samples are shown in **Figs. S10 – S14**. **(a, a') – (c, c')** and **(d, d') – (f, f')** F1s spectra for baseline and SrF_2 coated, **(g, g') – (i, i')** Sr3d spectra for SrF_2 coated.

To better understand the SrF_2 microspheres guided Li plating behavior, the First-principles calculations (CASTEP code) was employed to study the interaction between Li ion and the SrF_2 as presented in **Fig. 6**. To reveal the nature of Li ion adsorption the figure shows the calculated band structure and partial density of state (PDOS) of SrF_2 (110) plane with various adsorption sites. From **Fig. 6(a)**, there is a marked band separation between band structure and the valence band. The calculated band gap of SrF_2 (110) plane is 5.542 eV, which is smaller than that of the prefect SrF_2.[93] This discrepancy should be attributed to the unsaturated Sr and F atoms on the surface of SrF_2. According to the PDOS profile, the valence band of SrF_2 (110) plane is contributed by the F-2p state. However, the conduction band of SrF_2 (110) plane derives from the Sr-4d state. When Li ion is absorbed, it is found that the Li ion results in Sr-4d and F-2p state migration from the conduction band to the valence band. This result is in good agreement with the XPS results as shown in **Figs. 5(g) - (i)**, **5(g') - (i')**, **S14(e) - (f)** and **S14(e') – (f')**.

According to the structural configuration, we select the SrF_2 (110) surface and three possible adsorption models: Sr-top site, F-top site and Sr-F-bridge site, respectively. These results are shown in **Fig. 6(b**). The nature of Li ion adsorption is revealed by the electronic structure. **Table 2** lists the calculated adsorption energy and the corresponding bond length of SrF_2 with three adsorption types. The calculated adsorption energy on Sr-top site is larger than zero, which is energetically unfavorable. However, the calculated adsorption energy on F-top site or Sr-F-bridge is smaller than zero. These results show that SrF_2 with F-top site and Sr-F-bridge site are thermodynamically stable at the ground state. In particular, it is concluded that Li ion prefers to occupy the Sr-F-bridge site because the calculated adsorption energy on Sr-F-bridge site is the smallest. These findings are shown in **Fig. 6(c)**. We also can see that the calculated band gap of Sr-F bridge site is 0.323eV, per **Fig. 6(f)**. This value is smaller than that of Sr-top site and F-top sites. The calculated PDOS profile shows that there is the localized hybridization between Li ion and SrF_2 (110) plane, which is demonstrated by the variation of chemical bonding. This is displayed in the table.

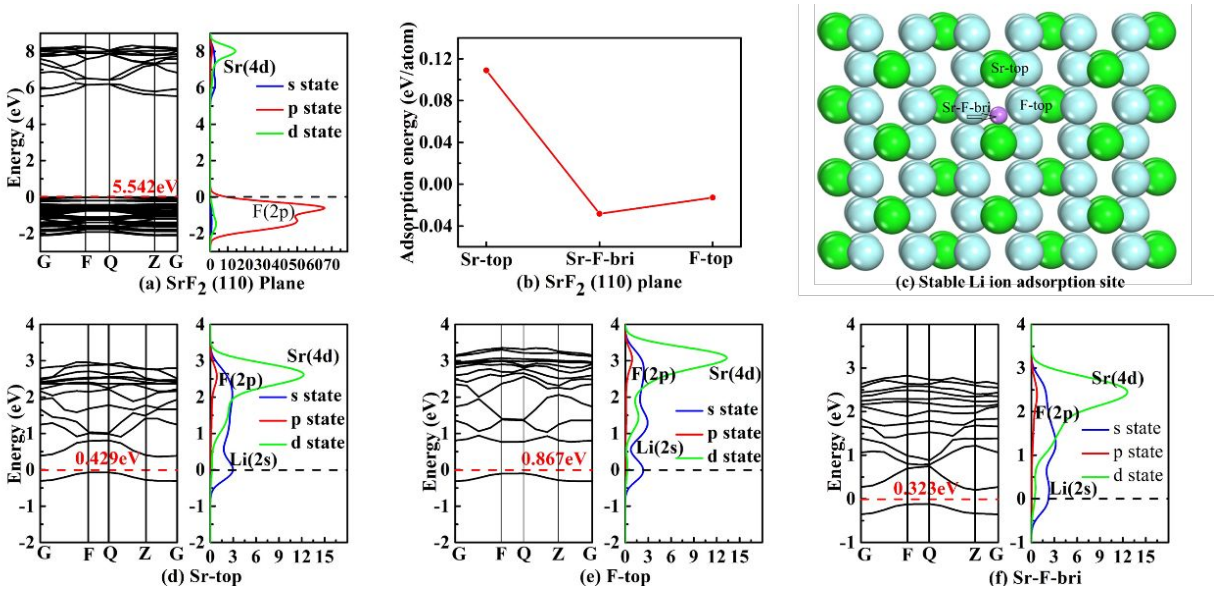

Figure 6. Calculated band structure and partial density of states for **(a)** SrF_2 (110) plane, **(d)** Sr-top site, **(e)** F-top site and **(f)** Sr-F-bridge site, respectively; **(b)** Surface energies of low index facets for SrF_2 (110) plane, and **(c)** stable lithium ion adsorption site on SrF_2 (110) plane.

Table 2. Calculated adsorption energy, E_f (eV/atom), bond length (Å) of SrF_2 with various adsorption types.

Type	Meth	E_f	Li-Sr	Li-F
Sr-top	Cal	0.1089	2.380	---
F-top	Cal	-0.0128	---	1.676
Sr-F-bridge	Cal	-0.0283	2.501	1.759

During the charging process of the Li||NCM cell, electrons transfer from the cathode to the surface of the Li metal anode through the external circuit. The SrF_2 microspheres are in contact with the Li metal would therefore be in the charged state. This should be effective in uniformly dispersing the Li cation flux onto the metal surface, reducing the propensity of localized heterogeneities to form, *i.e.* early state dendrites.[81] The ceramic non-conducting microspheres remain in a positive state of charge and homogenize the Li^+ flux at every cycle. This is balanced with the driving force for the ions to adsorb onto the exposed SrF_2 (110) planes, per the DFT calculations. In parallel, the SrF_2 microspheres involved in the formation

of SEI film also play the roles of rigid fillers, which will make the SEI film more compact and mechanically strong. It was demonstrated that the ceramic spheres bind with the SEI layer, creating an *in-situ* formed polymer-ceramic microcomposite that mechanically stabilizes a planar metal interface. **Figure 7** provides a comparison schematic for the SrF_2 coated versus the baseline separators, illustrating the core differences in resultant Li metal – electrolyte interfacial stability.

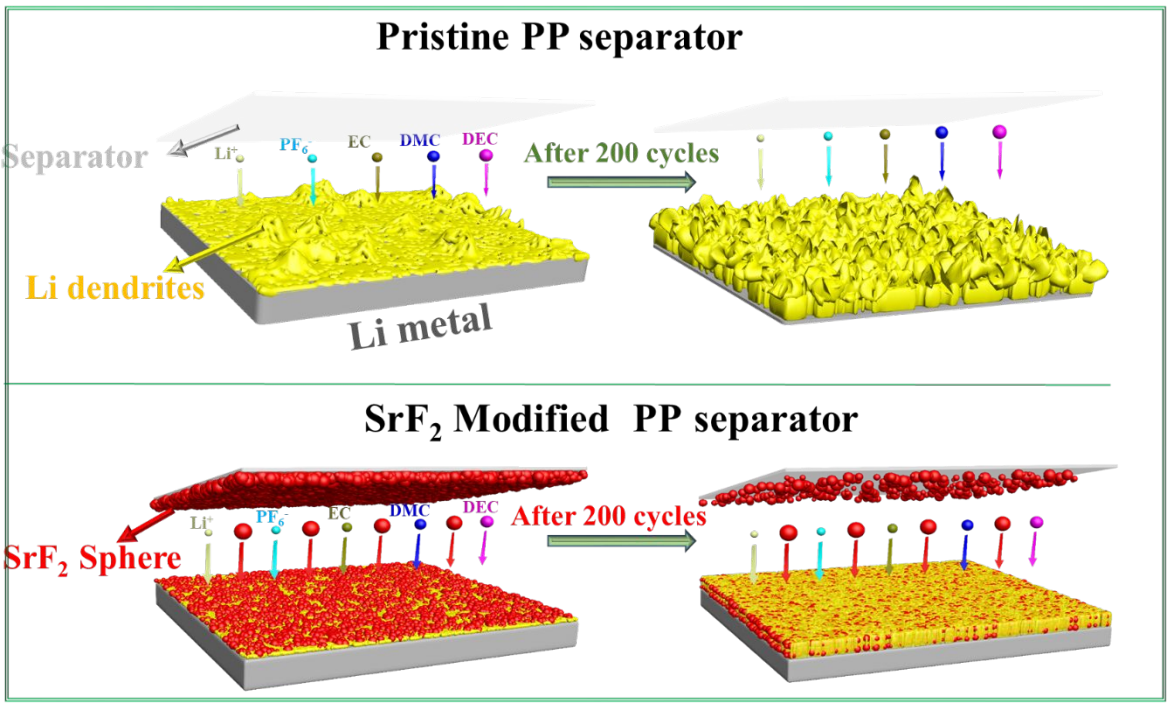

Figure 7 Schematic comparison of the post-200 cycles Li metal morphology in the baseline pristine PP separator (top) and the SrF_2 microspheres modified PP Separator (bottom).

A detailed comparison of this work with the previously reported separator studies is found in **Table 3**. A unique aspect of this study as compared to prior art is that the proposed dendrite prevention mechanism is both electrochemical and mechanical in nature, with the ceramic microparticles having a dual role.

Table 3. A broad comparison of various approaches for suppression of Li dendrites, with comments regarding the demonstrated or proposed working mechanisms.

Approach	Working Mechanisms	Refs.
Separator coated with functional SrF_2 microspheres	**Mechanical – electrochemical stabilization ceramic-SEI composite + homogenize of Li flux**	**This work**

Layer-by-layer assembling polyethylene oxide (PEO)	Smaller pore sizes to suppress the Li dendrites from piercing the separator	[55]
Elastomeric solid-electrolyte separator	Nanoporosity and high mechanical strength to suppress the Li dendrites piercing	[56]
Kimwipe paper	Uniform Li-ion distribution on the interface to suppress the Li dendrite growth	[60]
Coating separator with N,S-co-doped graphene nanosheets	High mechanical strength and uniform ionic flux to suppress the Li dendrite growth and piercing	[57]
Coating separator with Al_2O_3	High mechanical strength to suppress the Li from piercing the separator	[58]
Coating separator with conductive polymers,	Uniform interface and high ionic conductivity to suppress Li dendrite growth	[59]
Coating separator with functionalized nanocarbon	Controlling dendrites growth direction to suppress Li dendrites from piercing the separator	[61]
Coating separator with ultrathin Cu film	Conductive interface and high mechanical strength to suppress the Li dendrites growth and piercing	[62]
Coating separator with polydopamine	Uniform ionic flux to suppress Li dendrite growth	[63]
Coating separator with 3D porous ZSM-5	High ionic conductivity to suppress Li dendrite growth	[67]
Coating separator with ZrO_2/POSS	High ionic conductivity and interfacial stability to suppress Li dendrite growth	[68]

4. Conclusions

This work provides new experimental and theoretical insight regarding the function of separator ceramic coating layers in stabilizing the cycling and fast charge behavior of the metal anode – organic electrolyte interface. Strontium fluoride microsphere are employed to coat a conventional polypropylene separator, using an identical uncoated architecture as a baseline. Model Li||Cu and Li||Li cells, as well as for full-cell LMBs composed of an NMC cathode versus a Li metal anode were analyzed. The key finding is that the SrF_2 layer coated on the anode side will keep the plating/stripping metal from developing coarse dendrites by mechanically-electrochemically stabilizing the solid electrolyte interphase (SEI). This is achieved through *in-situ* creation of a tough composite membrane of SrF_2 microparticles imbedded within the SEI layer (mechanical), while the actual SrF_2 microspheres homogenize the Li ion flux around them (electrochemical). A substantial improvement in cycling CE and cycling voltage stability, rate capability, as well as in plating-stripping overpotential was observed. The discovered synergy between ceramic separator coatings,

mechanical-electrochemical stabilization of SEI, and mitigation of dendrite related failure may become a key LMB anode design rule.

Conflicts of interest

There are no conflicts to declare.

Acknowledgements

X.L, Y.L, Y.P., M.W., J.C., H.X., Y.H., W.M.L., A.S. and J.Z. (conception, experimental and modeling execution of research, preparation of manuscript) were supported by National Natural Science Foundation of China (grant no. 51474196, 51502250), the Science & Technology Department of Sichuan Province (grant no. 2017JQ0044), and the Southwest Petroleum University (grant no. 2015CXTD04). D.M. (guidance and interpretation of research, co-preparation of manuscript) was supported by the U.S. Department of Energy, Office of Basic Energy Sciences, Division of Materials Sciences and Engineering under Award # DE-SC0018074.

References

1. J. Zheng, M. H. Engelhard, D. Mei, S. Jiao, B. J. Polzin, J.-G. Zhang and W. Xu, *Nat. Energy*, 2017, **2**, 17012.
2. X. Li, J. Tao, D. Hu, M. H. Engelhard, W. Zhao, J.-G. Zhang and W. Xu, *J. Mater. Chem. A*, 2018, **6**, 5006-5015.
3. Y. Sun, N. Liu and Y. Cui, *Nat. Energy*, 2016, **1**, 16071.
4. X.-B. Cheng and Q. Zhang, *J. Mater. Chem. A*, 2015, **3**, 7207-7209.
5. X. B. Cheng, R. Zhang, C. Z. Zhao and Q. Zhang, *Chem. Rev.*, 2017, **117**, 10403-10473.
6. W. Xu, J. Wang, F. Ding, X. Chen, E. Nasybulin, Y. Zhang and J. G. Zhang, *Energy Environ. Sci.*, 2014, **7**, 513-537.
7. X. Li, J. Zheng, X. Ren, M. H. Engelhard, W. Zhao, Q. Li, J. G. Zhang and W. Xu, *Adv. Energy Mater.*, 2018, 1703022.
8. J.-G. Zhang, W. Xu and W. A. Henderson, Lithium Metal Anodes and Rechargeable Lithium Metal Batteries, Springer, 2017.

9. C.-Y. Tang and S. J. Dillon, *J. Electrochem. Soc.*, 2016, **163**, A1660-A1665.
10. H. Sano, M. Kitta and H. Matsumoto, *J. Electrochem. Soc.*, 2016, **163**, D3076-D3079.
11. P. Bai, J. Li, F. R. Brushett and M. Z. Bazant, *Energy Environ. Sci.*, 2016, **9**, 3221-3229.
12. J. Steiger, D. Kramer and R. Mönig, *Electrochim. Acta*, 2014, **136**, 529-536.
13. M. S. Park, S. B. Ma, D. J. Lee, D. Im, S. G. Doo and O. Yamamoto, *Sci. Rep.*, 2014, **4**, 3815.
14. M. Sun, H. G. Liao, K. Niu and H. Zheng, *Sci. Rep.*, 2013, **3**, 3227.
15. L. Chen, H. W. Zhang, L. Y. Liang, Z. Liu, Y. Qi, P. Lu, J. Chen and L.-Q. Chen, *J. Power Sources*, 2015, **300**, 376-385.
16. T. H. Lin, C. W. Lin, H. H. Liu, J. T. Sheu and W. H. Hung, *Chem. Commun.*, 2011, **47**, 2044-2046.
17. A. Aryanfar, D. J. Brooks, A. J. Colussi and M. R. Hoffmann, *Phys. Chem. Chem.Phys. : PCCP*, 2014, **16**, 24965-24970.
18. M. Lazzari, *J. Electrochem. Soc.*, 1980, **127**, 773-774.
19. M. D. Tikekar, S. Choudhury, Z. Tu and L. A. Archer, *Nat. Energy*, 2016, **1**, 16114.
20. D. Rehnlund, F. Lindgren, S. Böhme, T. Nordh, Y. Zou, J. Pettersson, U. Bexell, M. Boman, K. Edström and L. Nyholm, *Energy Environ. Sci.*, 2017, **10**, 1350-1357.
21. K. Zhang, G.-H. Lee, M. Park, W. Li and Y.-M. Kang, *Adv. Energy Mater.*, 2016, **6**, 1600811.
22. X. B. Cheng, R. Zhang, C. Z. Zhao, F. Wei, J. G. Zhang and Q. Zhang, *Adv. Sci.*, 2016, **3**, 1500213.
23. B. M. L. Rao, *J. Electrochem. Soc.*, 1977, **124**, 1490-1492.
24. K. Xu, *Chem. Rev.*, 2014, **114**, 11503-11618.
25. K. Xu, *Chem. Rev.*, 2004, **104**, 4303-4418.
26. E. Peled, *J. Electrochem. Soc.*, 1979, **126**, 2047-2051.
27. Q. Ma, Z. Fang, P. Liu, J. Ma, X. Qi, W. Feng, J. Nie, Y.-S. Hu, H. Li, X. Huang, L. Chen and Z. Zhou, *ChemElectroChem*, 2016, **3**, 531-536.
28. J. Zheng, J. A. Lochala, A. Kwok, Z. D. Deng and J. Xiao, *Adv. Sci.*, 2017, **4**, 1700032.
29. S.-K. Jeong, H.-Y. Seo, D.-H. Kim, H.-K. Han, J.-G. Kim, Y. B. Lee, Y. Iriyama, T. Abe and Z. Ogumi, *Electrochem. Commun.*, 2008, **10**, 635-638.
30. Y. Yamada and A. Yamada, *J. Electrochem. Soc.*, 2015, **162**, A2406-A2423.

31. Z. Tu, P. Nath, Y. Lu, M. D. Tikekar and L. A. Archer, *Acc. Chem. Res.*, 2015, **48**, 2947-2956.
32. M. D. Tikekar, L. A. Archer and D. L. Koch, *Sci. Adv.*, 2016, **2**, e1600320.
33. M. D. Tikekar, L. A. Archer and D. L. Koch, *J. Electrochem. Soc.*, 2014, **161**, A847-A855.
34. S. L. Koch, B. J. Morgan, S. Passerini and G. Teobaldi, *J. Power Sources*, 2015, **296**, 150-161.
35. L. Shi, A. Xu and T. Zhao, *ACS Appl. Mater. Interfaces*, 2017, **9**, 1987-1994.
36. H.-K. Jing, L.-L. Kong, S. Liu, G.-R. Li and X.-P. Gao, *J. Mater. Chem. A*, 2015, **3**, 12213-12219.
37. M. Gauthier, T. J. Carney, A. Grimaud, L. Giordano, N. Pour, H.-H. Chang, D. P. Fenning, S. F. Lux, O. Paschos and C. Bauer, *J. Phys. Chem. Lett.*, 2015, **6**, 4653-4672.
38. Z. Peng, S. Wang, J. Zhou, Y. Jin, Y. Liu, Y. Qin, C. Shen, W. Han and D. Wang, *J. Mater. Chem. A*, 2016, **4**, 2427-2432.
39. L. Li, S. Basu, Y. Wang, Z. Chen, P. Hundekar, B. Wang, J. Shi, Y. Shi, S. Narayanan and N. Koratkar, *Science*, 2018, **359**, 1513-1516.
40. P. Bai, J. Li, F. R. Brushett and M. Z. Bazant, *Energy Environ. Sci.*, 2016, **9**, 3221-3229.
41. W. Liu, P. Li, W. Wang, D. Zhu, Y. Chen, S. Pen, E. Paek and D. Mitlin, *ACS nano*, 2018, **12**, 12255-12268.
42. W. Liu, Y. Xia, W. Wang, Y. Wang, J. Jin, Y. Chen, E. Paek and D. Mitlin, *Adv. Energy Mater.* 2019, **9**, 1802918.
43. R. Chen, W. Qu, X. Guo, L. Li and F. Wu, *Mater. Horiz.*, 2016, **3**, 487-516.
44. A. Manthiram, X. Yu and S. Wang, *Nat. Rev. Mater.*, 2017, **2**, 16103.
45. V. Thangadurai, S. Narayanan and D. Pinzaru, *Chem. Soc. Rev.*, 2014, **43**, 4714-4727.
46. Z. Lin and C. Liang, *J. Mater. Chem. A*, 2015, **3**, 936-958.
47. M. Motoyama, M. Ejiri and Y. Iriyama, *J. Electrochem. Soc.*, 2015, **162**, A7067-A7071.
48. Y. S. Hu, *Nat. Energy*, 2016, **1**, 16042.
49. Q. Guo, Y. Han, H. Wang, X. Hong, C. Zheng, S. Liu and K. Xie, *Rsc Adv.*, 2016, **6**.
50. W. Zhou, Z. Wang, Y. Pu, Y. Li, S. Xin, X. Li, J. Chen and J. B. Goodenough, *Adv. Mater.*, 2019, **31**, 1805574.
51. H. Gao, S. Xin, L. Xue and J. B. Goodenough, *Chem*, 2018, **4**, 833-844.
52. B. Lee, E. Paek, D. Mitlin and S. W. Lee, *Chem. Rev.*, 2019, **119**, 5416-5460.

53. Z. Liang, G. Zheng, C. Liu, N. Liu, W. Li, K. Yan, H. Yao, P. C. Hsu, S. Chu and Y. Cui, *Nano Lett.*, 2015, **15**, 2910-2916.
54. X. B. Cheng, T. Z. Hou, R. Zhang, H. J. Peng, C. Z. Zhao, J. Q. Huang and Q. Zhang, *Adv. Mater.*, 2016, **28**, 2888-2895.
55. Y. Liu, D. Lin, Z. Liang, J. Zhao, K. Yan and Y. Cui, *Nat. Commun.*, 2016, **7**, 10992.
56. D. Lin, Y. Liu, Z. Liang, H. W. Lee, J. Sun, H. Wang, K. Yan, J. Xie and Y. Cui, *Nat. Nanotech.*, 2016, **11**, 626-632.
57. C. P. Yang, Y. X. Yin, S. F. Zhang, N. W. Li and Y. G. Guo, *Nat. Commun.*, 2015, **6**, 8058.
58. A. Zhamu, G. Chen, C. Liu, D. Neff, Q. Fang, Z. Yu, W. Xiong, Y. Wang, X. Wang and B. Z. Jang, *Energy Environ. Sci.*, 2012, **5**, 5701-5707.
59. H. Ye, S. Xin, Y. X. Yin, J. Y. Li, Y. G. Guo and L. J. Wan, *J. Am. Chem. Soc.*, 2017, **139**, 5916-5922.
60. Q. Li, S. Zhu and Y. Lu, *Adv. Funct. Mater.*, 2017, **27**, 1606422.
61. R. Zhang, X. R. Chen, X. Chen, X. B. Cheng, X. Q. Zhang, C. Yan and Q. Zhang, *Angew. Chem. Int. Ed.*, 2017, **56**, 7764-7768.
62. S. Suriyakumar, A. M. Stephan, N. Angulakshmi, M. H. Hassan and M. H. Alkordi, *J. Mater. Chem. A*, 2018, **6**, 14623-14632.
63. M. Li, Y. Wan, J.-K. Huang, A. H. Assen, C.-E. Hsiung, H. Jiang, Y. Han, M. Eddaoudi, Z. Lai and J. Ming, *ACS Energy Lett.*, 2017, **2**, 2362-2367.
64. S. O. Tung, S. Ho, M. Yang, R. Zhang and N. A. Kotov, *Nat. Commun.*, 2015, **6**, 6152.
65. K. Liu, P. Bai, M. Z. Bazant, C. A. Wang and J. Li, *J. Mater. Chem. A*, 2017, **5**, 4300-4307.
66. W. K. Shin, A. G. Kannan and D. W. Kim, *ACS Appl. Mater. Interfaces*, 2015, **7**, 23700-23707.
67. H. Jeon, S. Y. Jin, W. H. Park, H. Lee, H.-T. Kim, M.-H. Ryou and Y. M. Lee, *Electrochim. Acta*, 2016, **212**, 649-656.
68. S. H. Lee, J. R. Harding, D. S. Liu, J. M. D'Arcy, Y. Shao-Horn and P. T. Hammond, *Chem. Mater.*, 2014, **26**, 2579-2585.
69. C.-H. Chang, S.-H. Chung and A. Manthiram, *Adv. Sustainable Syst.*, 2017, **1**, 1600034.
70. Y. Liu, Q. Liu, L. Xin, Y. Liu, F. Yang, E. A. Stach and J. Xie, *Nat. Energy*, 2017, **2**, 17083.

71. H. Lee, X. Ren, C. Niu, L. Yu, M. H. Engelhard, I. Cho, M.-H. Ryou, H. S. Jin, H.-T. Kim, J. Liu, W. Xu and J.-G. Zhang, *Adv. Funct. Mater.*, 2017, **27**, 1704391.
72. M.-H. Ryou, D. J. Lee, J.-N. Lee, Y. M. Lee, J.-K. Park and J. W. Choi, *Adv. Energy Mater.*, 2012, **2**, 645-650.
73. L. Wei, D. Lin, A. Pei and C. Yi, *J. Am. Chem. Soc.*, 2016, **138**, 15443-15450.
74. L. Yang, J. Zeng, B. Ding, C. Xu and J. Y. Lee, *Adv. Mater. Interfaces*, 2016, **3**, 1600660.
75. B.-C. Yu, K. Park, J.-H. Jang and J. B. Goodenough, *ACS Energy Lett.*, 2016, **1**, 633-637.
76. X. Mao, L. Shi, H. Zhang, Z. Wang, J. Zhu, Z. Qiu, Y. Zhao, M. Zhang and S. Yuan, *J. Power Sources*, 2017, **342**, 816-824.
77. M. Chi, L. Shi, Z. Wang, J. Zhu, X. Mao, Y. Zhao, M. Zhang, L. Sun and S. Yuan, *Nano Energy*, 2016, **28**, 1-11.
78. J. Li, L. Wang, Q. Zhang and X. He, *J. Power Sources*, 2009, **190**, 149-153.
79. X. Li, X. Zhao, P.-x. Huang, M.-s. Wang, Y. Huang, Y. Zhou, Y.-h. Lin, M.-z. Qu and Z.-l. Yu, *J. Alloys Compd.*, 2017, **693**, 61-69.
80. X. Li, K. Zhang, S. Wang, M. Wang, F. Jiang, Y. Liu, Y. Huang and J. Zheng, *Sustain. Energ. Fuels*, 2018, **2**, 1772-1780.
81. X. B. Cheng, M. Q. Zhao, C. Chen, A. Pentecost, K. Maleski, T. Mathis, X. Q. Zhang, Q. Zhang, J. Jiang and Y. Gogotsi, *Nat. Commun.*, 2017, **8**, 336.
82. F. Ding, W. Xu, G. L. Graff, J. Zhang, M. L. Sushko, X. Chen, Y. Shao, M. H. Engelhard, Z. Nie, J. Xiao, X. Liu, P. V. Sushko, J. Liu and J. G. Zhang, *J. Am. Chem. Soc.*, 2013, **135**, 4450-4456.
83. X. Li, J. Zheng, M. H. Engelhard, D. Mei, Q. Li, S. Jiao, N. Liu, W. Zhao, J.-G. Zhang and W. Xu, *ACS Appl. Mater. Interfaces*, 2018, **10**, 2469-2479.
84. E. Markevich, K. Fridman, R. Sharabi, R. Elazari, G. Salitra, H. E. Gottlieb, G. Gershinsky, A. Garsuch, G. Semrau, M. A. Schmidt and D. Aurbach, *J. Electrochem. Soc.*, 2013, **160**, A1824-A1833.
85. F. Amalraj, M. Talianker, B. Markovsky, L. Burlaka, N. Leifer, G. Goobes, E. M. Erickson, O. Haik, J. Grinblat, E. Zinigrad, D. Aurbach, J. K. Lampert, J.-Y. Shin, M. Schulz-Dobrick and A. Garsuch, *J. Electrochem. Soc.*, 2013, **160**, A2220-A2233.
86. O. Yariv, D. Hirshberg, E. Zinigrad, A. Meitav, D. Aurbach, M. Jiang and B. R. Powell, *J. Electrochem. Soc.*, 2014, **161**, A1422-A1431.

87. J. Zheng, W. Shi, M. Gu, J. Xiao, P. Zuo, C. Wang and J.-G. Zhang, *J. Electrochem. Soc.*, 2013, **160**, A2212-A2219.
88. X. Li, Y. Tang, J. Song, W. Yang, M. Wang, C. Zhu, W. Zhao, J. Zheng and Y. Lin, *Carbon*, 2018, **129**, 236-244.
89. X. Li, K. Zhang, D. Mitlin, E. Paek, M. Wang, F. Jiang, Y. Huang, Z. Yang, Y. Gong, L. Gu, W. Zhao, Y. Du and J. Zheng, *Small*, 2018, **14**, e1802570.
90. X. Li, K. Zhang, D. Mitlin, Z. Yang, M. Wang, Y. Tang, F. Jiang, Y. Du and J. Zheng, *Chem. Mater.*, 2018, **30**, 2566-2573.
91. H. Ota, Y. Sakata, A. Inoue and S. Yamaguchi, *J. Electrochem. Soc.*, 2004, **151**, A1659.
92. C. K. Chan, R. Ruffo, S. S. Hong and Y. Cui, *J. Power Sources*, 2009, **189**, 1132-1140.
93. H. D. W. W. Weiss, and W. Gopel, *Phys. Rev.*, 1992, **45**.